

Comprehensive peak-width analysis in matter-wave diffraction under grazing incidence conditions

Lee Yeong Kim,¹ Do Won Kang,² Jong Chan Lee,² Eunmi Chae,³ Wieland Schöllkopf,^{4,*} and Bum Suk Zhao (조범석)^{1,2,†}

¹*Department of Physics, Ulsan National Institute of Science and Technology (UNIST), Ulsan 44919, Republic of Korea*
²*Department of Chemistry, Ulsan National Institute of Science and Technology (UNIST), Ulsan 44919, Republic of Korea*

³*Department of Physics, Korea University, Seongbuk-gu, Seoul, Republic of Korea*

⁴*Fritz-Haber-Institut der Max-Planck-Gesellschaft, Faradayweg 4-6, 14195 Berlin, Germany*

(Dated: November 22, 2023)

Thermal energy atom scattering at a surface with grazing incidence conditions is an innovative method for investigating dispersive atom–surface interactions, with potential application in quantum sensing interferometry. The complete establishment of this technique requires a detailed peak analysis, which has yet to be achieved. We examined peak-width fluctuations in atomic and molecular beams diffracted by a grating under grazing incidence conditions. Careful measurements and analyses of the diffraction patterns of He atoms and D₂ molecules from three square-wave gratings with different periods and radii of curvature enabled the identification of factors influencing the variations in the width as a function of the grazing incidence angle. The effects of macroscopic surface curvature, grating magnification, and beam emergence are substantial under these conditions but negligible when the incidence angles are close to normal. Our results will shed light on phenomena occurring in grazing incident thermal energy atom scattering.

X-ray, electron, neutron, and atom diffraction techniques are well-established methods for studying the crystal structures of materials and their changes over time. In diffraction experiments, the width of the diffraction peak, along with its intensity and position, is a critical parameter for sample analysis. For instance, peak-width analysis has been employed to estimate crystallite or grain sizes and crystal strains in X-ray powder diffraction [1–4] and in grazing incidence X-ray scattering [5, 6]. In thermal-energy atom scattering (TEAS), the broadening of peak widths provides insights into temperature-induced alterations in surface morphology [7], the density of defects, such as steps on a crystal surface [8, 9], and the width of the atom beam velocity distribution [10].

The design of optical elements, such as mirrors and gratings, for X-ray and matter-wave optics also necessitates a comprehensive investigation of scattering peak widths. Efficient focusing of X-rays has been accomplished using cylindrical concave mirrors by minimizing broadening effects [11–13]. Recently, this endeavor has also been extended to He atoms [14]. Furthermore, understanding wavelength-dependent peak width broadening is essential for atom monochromators [15]. Thus, analyzing peak widths is crucial for developing new methodologies and technologies based on the wave diffraction phenomenon.

Grazing incidence thermal energy atom scattering (GITEAS) at a surface is a novel technique that could complement conventional TEAS, analogous to the relationship between X-ray scattering and grazing incidence X-ray scattering. The smaller effective energy and longer wavelength toward the surface for GITEAS make it sensitive to weak interactions and insensitive to surface roughness. Thus, GITEAS has emerged as a novel method

for studying the dispersive interaction of atoms with a surface [16–18]. Furthermore, microstructure-grating interferometry with GITEAS can be used for quantum sensing, alongside monolithic atom interferometry with TEAS [19]. However, under grazing incidence conditions, the peak widths are strongly influenced by an infinitesimal curvature (curvature radius of a few kilometers) and the diffraction direction near a surface; consequently, the traditional peak-width analysis scheme for TEAS is inapplicable to GITEAS. Because research on GITEAS is still in its early stages, a comprehensive analysis of peak widths has not yet been reported.

In this study, we measured and analyzed the peak widths of matter-wave beams scattering off a grating under grazing incidence conditions. By adjusting the grating and incident beam properties, we investigated various factors contributing to peak-width variations, such as the macroscopic surface curvature, grating magnification, incident beam divergence, and angular dispersion. He atoms (D₂ molecules) with mean de Broglie wavelengths λ of 330 or 140 pm (140 pm) were diffracted at grazing incidence angles up to 30 mrad by three gratings of different periods and macroscopic curvatures. By comparing the measured peak widths with calculated ones, we identified the dominant factors influencing the peak-width variations.

An atom optics setup, characterized by a tightly collimated incident beam and high-angular-resolution detector, facilitates precise measurements of peak widths. Detailed information about the configuration can be found in previous references [17, 20] and Supplemental Material [21]. Here, we focused on the aspects of the apparatus pertinent to the data analysis presented in this study. A continuous beam of He or D₂ was formed from a supersonic

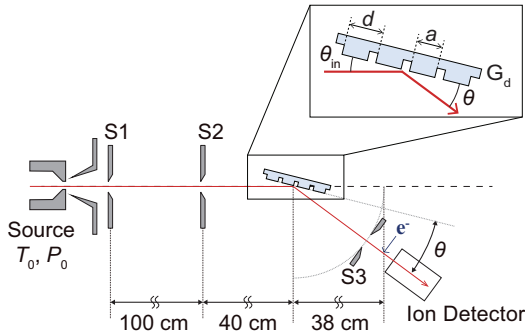


FIG. 1. Schematic of the experimental setup. The distances between the components are not drawn to scale. The incidence and detection angles, θ_{in} and θ , are measured with respect to the grating surface. The inset illustrates a grating with d and a representing its period and strip width, respectively.

expansion of the corresponding pure gas from a source cell. The source temperature (T_0) and pressure (P_0) influence particle velocity distributions. We used three sets of source conditions, viz. gas species, T_0 , and P_0 : (He, 9.0 K, 0.5 bar), (He, 52 K, 26 bar), and (D_2 , 52 K, 1 bar). For each condition set, we obtained a velocity distribution, from which the mean velocity (v), full width at half maximum (FWHM) (Δv), and corresponding λ (see Fig. S1 [21]) were determined. Accordingly, we obtained three corresponding sets of incidence beam properties, including λ , v , and Δv : (330 pm, 304 m/s, 2.3 m/s), (140 pm, 733 m/s, 5.9 m/s), and (140 pm, 736 m/s, 79 m/s), respectively, which were used to explore the effects of λ and Δv separately.

The collimation of the beam was achieved using two slits (S1 and S2), which were positioned 100 cm apart as shown in Fig. 1. The widths of these slits, W_{S1} and W_{S2} , were the same (20 μm). The incident and scattered beams were detected by precisely rotating a mass spectrometer with electron-bombardment ionization. The rotational axis of the detector was located 40 cm downstream from S2. Just before the ion detector, a third slit (S3) with a width of $W_{\text{S3}} = 25 \mu\text{m}$ was positioned. The distance between the rotational axis and S3, referred to as the grating-detector distance (or detector radius), was $L = 38 \text{ cm}$. This distance, combined with the narrow S3, yielded an FWHM of approximately 120 μrad for the collimated incident beam.

We employed three square-wave gratings with varying periods d and strip widths a : G_1 with $d = 1 \mu\text{m}$ and $a = 0.25 \mu\text{m}$; G_{20} with $d = 20 \mu\text{m}$ and $a = 10 \mu\text{m}$; and G_{400} with $d = 400 \mu\text{m}$ and $a = 200 \mu\text{m}$. Although a grating is spherically curved, the curvature along the direction perpendicular to the incident plane only negligibly affects the peak width under grazing incidence conditions [22, 23]. Therefore, these gratings were considered cylindrical, with their curvature radii R . For concave and convex gratings, $R > 0$ and $R < 0$, respectively. The esti-

mated R values of G_1 , G_{20} , and G_{400} were 30, -210 , and 1800 m , respectively. Together with the different λ and Δv values, these characteristics of the gratings allowed us to evaluate the aforementioned factors, which affect peak-width variations.

We measured the angular spectra representing the He signal as a function of the detection angle θ (see Fig. S2 for an example [21]). A peak in a spectrum corresponds to a specific diffraction order. The peak positions θ_n and FWHM values w_n of the n th-order diffraction beams were determined by fitting each peak to with a single Gaussian function. Similarly, we determined the FWHM w_{in} of the incident beam spectrum when the grating was moved away from the beam path.

Fig. 2 shows w_n of the matter-wave beams diffracted from the three gratings, (a) G_1 , (b) G_{20} , and (c)–(e) G_{400} , against θ_{in} . Each graph includes horizontal dotted lines, which indicate the width of the incident beam (w_{in}), and vertical dashed lines, which represent the Rayleigh incidence angle of the -1 st-order diffraction beam ($\theta_{R,-1}$). When $\theta_{\text{in}} = \theta_{R,-1}$, the -1 st-order diffraction beam emerges from the grating and propagates parallel to it; in this case, $\theta_{-1} = 0$ [24, 25].

The behavior of w_n as it varies with θ_{in} varies under different experimental conditions and for individual diffraction orders. Furthermore, the hierarchy among w_0 , w_1 , and w_{-1} at a given θ_{in} is not consistent and changes with θ_{in} . Several factors contribute to these variations: (i) the macroscopic curvature of the grating surface, (ii) grating magnification, (iii) diffraction beam spread resulting from the divergence of the incident beam, (iv) angular dispersion due to the non-monochromatic nature of the beam, and (v) relative vertical orientation of the grating with respect to S2 and S3. Among these factors, (i) pertains to a property of the grating, (ii) results from the diffraction principle, (iii) and (iv) are characteristics of the incident beam, while (v) is associated with systematic errors. Briefly, the curvature of the grating surface accounts for the variation in w_0 shown in Fig. 2. The magnitude of $|R|$ directly influences the steepness of the decrease in w_0 . Additionally, when $R > 0$ ($R < 0$), w_0 increases (decreases) asymptotically toward w_{in} with θ_{in} , as illustrated in Fig. 2(a) [Fig. 2(b)]. Furthermore, the steep increase in w_{-1} with decreasing θ_{in} in Fig. 2(a) and 2(e) is attributed to angular dispersion. Finally, the hierarchical order of $w_1 > w_0 > w_{-1}$ shown in the inset of Fig. 2(d) results from the grating magnification. See below for more details.

Factors (i)–(iv) contribute to w_n differently depending on n , λ , and θ_{in} , which can be formulated by the following approximate equation for a linear width $W_n = Lw_n$: $W_n = \sqrt{[W_n^{(1)}]^2 + [W_n^{(2)}]^2 + [W_n^{(3)}]^2 + [W_n^{(4)}]^2 + [W_n^{(5)}]^2}$,

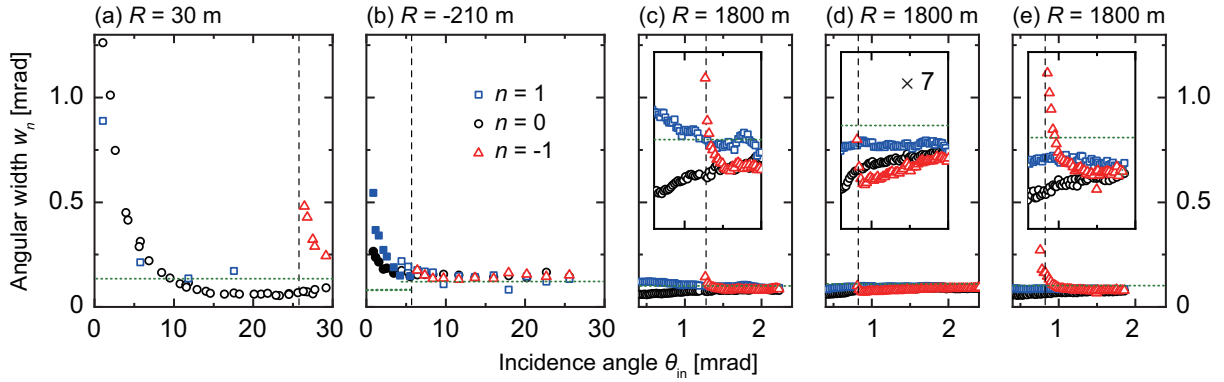


FIG. 2. Angular FWHM of the n th-order diffraction peak, w_n , as a function of the incidence angle θ_{in} . The experimental data are acquired using (a) G_1 , (b) G_{20} , and (c)–(e) G_{400} . The mean wavelengths λ of the incident beams are 330 pm for (a)–(c) and 140 pm for (d) and (e). For (a)–(d), the incident particles are He atoms, whereas for (e), they are D_2 molecules. The vertical dashed line denotes the Rayleigh incidence angle of the -1 st-order diffraction beam, referred to as $\theta_{R,-1}$, where the -1 st-order diffraction beam emerges from the grating surface. The horizontal dotted line represents the width of the incident beam, w_{in} . In (b), filled symbols within the range of θ_{in} from 0.5 to 5.5 mrad illustrate data obtained with tight collimation, resulting in a narrower w_{in} of 0.081 mrad (thick horizontal line). Insets in (c)–(e) provide seven-fold magnifications of the corresponding data series.

where

$$W_n^{(1)} = \left(\frac{1}{o} + \frac{1}{L} - \frac{1}{f_n} \right) LW_G \frac{\sin \theta_n}{\sin \theta_{\text{in}}}, \quad (1)$$

$$W_n^{(2)} = \frac{2.355}{4} \frac{W_{S1}}{o} L \frac{\sin \theta_{\text{in}}}{\sin \theta_n}, \quad (2)$$

$$W_n^{(3)} = 0.884 \frac{\lambda}{W_{S2}} L \frac{\sin \theta_{\text{in}}}{\sin \theta_n}, \quad (3)$$

$$W_n^{(4)} = \left(\frac{|n|\lambda}{d} \right) \frac{\Delta v}{v} \frac{1}{\sin \theta_n} L, \quad (4)$$

and

$$W_n^{(5)} = \frac{2.355}{4} W_{S3}. \quad (5)$$

These five terms of W_n correspond to the FWHM values for their respective contributions and are assumed to be random and independent. In these equations, o represents the object distance, f_n stands for the focal length of the n th-order diffraction beam, and W_G denotes the width of the incidence beam at the center of the grating. Because $S1$ constrains the effective source size of the matter-wave beam, we approximate the object as a Gaussian distribution with a standard deviation of $W_{S1}/4$. Similarly, the boxcar-shaped function defined by $S3$ is approximated as a Gaussian function with a standard deviation of $W_{S3}/4$.

The macroscopic curvature of the grating represented by R is relevant to its focal length. Under grazing incidence conditions, the object distance o and image distance i_n of the n th-order beam satisfy the thin lens equation: $1/o + 1/i_n = 1/f_n$. The term in the parentheses of

Eq. (1) then represents the focusing error, ϵ_n , and the product $\epsilon_n L W_G$ is the width of the defocused incidence beam at the detection plane [26]. The focal length f_n is a function of R and θ_{in} . Specifically, f_0 can be expressed as $f_0 = R \sin \theta_{\text{in}}/2$ [11, 14]; therefore, i_n (or ϵ_n) can be determined based on the values of R and θ_{in} , as illustrated in Fig. S3 [21].

The grating magnification $M_n = \sin \theta_n / \sin \theta_{\text{in}}$, also known as anamorphic magnification, represents the ratio of the width of a collimated diffracted beam to that of a collimated incident beam [27]. When considering a collimated beam ($o \rightarrow \infty$) incident on a flat grating ($f_n \rightarrow \infty$), $W_n^{(1)}$ characterizes the grating magnification.

$W_n^{(2)}$ is relevant to the effect of the geometrical incidence beam divergence $\Delta \theta_{\text{in},\text{GO}} \simeq W_{S1}/o$ on the diffraction beam spread $\Delta \theta_n$. When $W_{S1} = 20 \mu\text{m}$, $W_n^{(2)} = 3.2 \mu\text{m}$ for the specular peak, which is negligible. In contrast, $W_n^{(2)}$ becomes significant when $\theta_{n<0} \rightarrow 0$ as θ_{in} decreases to $\theta_{R,m}$.

The diffraction at $S2$ introduces additional incidence beam divergence $\Delta \theta_{\text{in},\text{SD}}$. Generally, the Fresnel number F governs the characteristics of single-slit diffraction. When $F \gg 1$, the diffraction pattern closely resembles a perfect shadow of $S2$. When $F \simeq 1$, the FWHM of the diffraction pattern becomes smaller than W_{S2} [26]. Hence, in such conditions, the influence of slit diffraction ($W_n^{(3)}$) can be disregarded, implying that $W_n^{(3)} = 0$. Conversely, when $F \ll 1$, a Fraunhofer pattern is produced, characterized by a sinc function with a diverging angle of $\Delta \theta_{\text{in},\text{SD}} = 0.844\lambda/W_{S2}$. Similar to $W_n^{(2)}$, this contribution is minimal for the specular beam but becomes pronounced for emerging orders. Therefore, we must consider $W_n^{(3)}$ when both F and $\theta_{n<0}$ are very small.

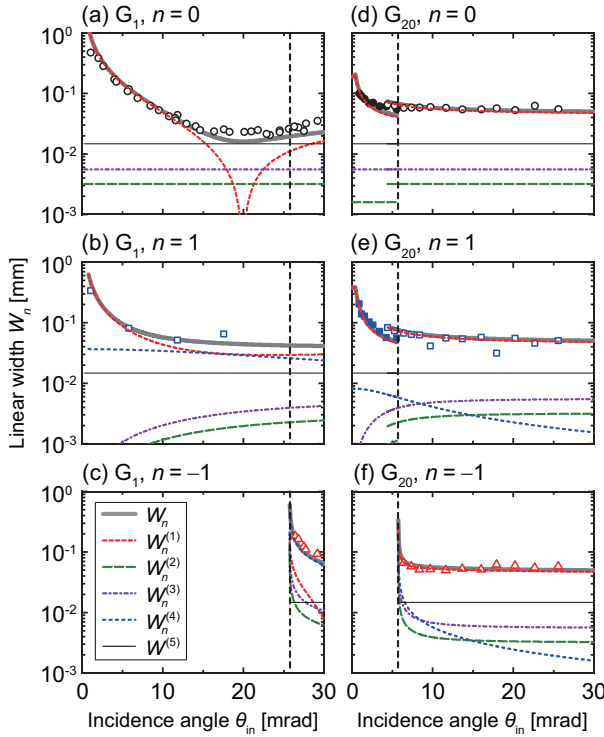


FIG. 3. Comparison between the measured (symbols) and calculated (solid curves) linear widths W_n of the n th-order diffraction beam. The first- and second-column data are for G_1 and G_{20} , respectively. The data are listed sequentially from the top for $n = 0, 1$, and -1 . W_0 , W_1 , and W_{-1} are plotted separately with the calculated $W_n^{(1)}$, $W_n^{(2)}$, $W_n^{(3)}$, $W_n^{(4)}$, and $W_n^{(5)}$.

$W_n^{(4)}$ accounts for the broadening of the diffraction peak due to angular dispersion. This effect is absent in the specular peak.

The finite size of the detector entrance slit, S3, also contributes to the broadening of the diffraction peak ($W_n^{(5)}$), as formulated in Eq. (5). This contribution is $15 \mu\text{m}$ for all experimental conditions.

To assess the relative contributions of these five terms to W_n , in Fig. 3 we compared the measured W_n (symbols) for G_1 and G_{20} with the corresponding calculated values for W_n , $W_n^{(1)}$, $W_n^{(2)}$, $W_n^{(3)}$, $W_n^{(4)}$, and $W_n^{(5)}$ (lines). These theoretical curves are determined considering R as the sole adjustable parameter. The angular width w_n presented in Figs. 2(a) and 2(b) is converted to the linear width and presented in the first- and second-column graphs in Fig. 3, respectively. The values for $W_n^{(1)}$ corresponding to G_1 (G_{20}) are calculated with $W_G = 34.6 \mu\text{m}$ ($W_G = 34.2 \mu\text{m}$). The estimation of W_G employs the linear width of the incidence beam, namely, $W_{\text{in}} = 45.6 \mu\text{m}$ ($W_{\text{in}} = 46.0 \mu\text{m}$). Note that two data sets exist for G_{20} . The collimation conditions differ between the data at $\theta_{\text{in}} < 5.5 \text{ mrad}$ (filled symbols) and the remaining data (open symbols). For the former, W_{S1} and W_{S2} are set to

10 and $15 \mu\text{m}$, respectively, resulting in $w_{\text{in}} = 81 \mu\text{rad}$ ($W_{\text{in}} = 30.8 \mu\text{m}$ and $W_G = 21.2 \mu\text{m}$). Figures 3(d)–3(f) also illustrate the corresponding calculations.

The breakdown of W_n into its five constituent terms in Fig. 3 highlights the dominant factor in each case. The substantial reductions in W_n for G_1 at varying incidence angles result from different factors for $n = 0, 1$, and -1 . As illustrated in the left-column graphs, at $\theta_{\text{in}} < 10 \text{ mrad}$, $\theta_{\text{in}} < 5 \text{ mrad}$, and $\theta_{\text{in}} < 30 \text{ mrad}$, $W_0^{(1)}$, $W_1^{(1)}$ (red dashed curves), and $W_{-1}^{(4)}$ (blue-dotted curve) predominantly influence their respective W_n values. Notably, the grating magnification is unity for the specular beam, making ϵ_0 the key determinant for $W_0^{(1)}$. Conversely, ϵ_1 varies by less than 33% in the given range of incidence angles while M_1 decreases tenfold [see Figs. S3(c1) and S3(d1)] [21]. Therefore, the principal contributors to the steep reductions in W_n for $n = 0, 1$, and -1 are the macroscopic curvature, grating magnification, and angular dispersion, respectively.

Similar to G_1 , the decrease in W_0 and W_1 for G_{20} is primarily determined by the macroscopic curvature and grating magnification, respectively [see Figs. 3(d), 3(e), S4(c2), and S4(d2)]. However, unlike G_1 , the 20-fold larger d of G_{20} diminishes the effect of angular dispersion [see Eq. (4)], and as a result, the influence of curvature on the reduction of W_{-1} becomes dominant.

Even though G_{400} is nearly flat with $R = 1800 \text{ m}$, the curvature still affects the variation in peak width. The narrowing of w_0 and w_1 relative to w_{in} in Figs. 2(c)–2(e) demonstrates the impact of curvature (refer to the first row in Fig. S4) [21].

The hierarchy of widths due to the grating magnification for G_{400} in Figs. 2(c) and 2(e) is not as consistent as that in Fig. 2(d). While $w_1 > w_0$ at the given incidence angles, w_{-1} is not consistently the narrowest. Specifically, when θ_{in} is slightly larger than $\theta_{R,-1}$, w_{-1} exceeds both w_0 and w_1 . As shown in Figs. S4(c), S4(f), and S4(i), the broader w_{-1} , namely, W_{-1} , results from the larger contributions of $W_{-1}^{(2)}$ (long-dashed green line), $W_{-1}^{(3)}$ (violet dash-dotted line), and $W_{-1}^{(4)}$ (blue-dotted line) compared with $W_{-1}^{(1)}$ (red-dashed line). The small θ_{-1} at this near-Rayleigh condition amplifies these three terms. Interestingly, as shown in Fig. S4, $W_{-1}^{(2)}$ and $W_{-1}^{(3)}$ are the dominant factors for the He atom beams with two different λ , whereas $W_{-1}^{(4)}$ is the crucial factor for the D_2 molecular beam. This behavior can be attributed to the 13-times larger Δv value of the D_2 beam compared with that of the He beam at the same v .

In conclusion, our combined experimental and theoretical investigations of diffraction peak widths in GITEAS revealed the primary factors that induce variations in the peak width. Notably, the primary factor that governs the width of diffraction beams varies depending on the diffraction order, incidence angle, and grating period. Our study reveals the effects of macroscopic curvature,

emerging beams, and grating magnification, which have been overlooked in other scattering techniques, such as TEAS. Furthermore, a specular peak narrower than the incident beam (see Figs. 2(c)–2(e)) indicates that the effect of surface defects is negligible in GITEAS, while it is the main cause of peak broadening in TEAS [28].

The detailed analysis may provide insights into the experimental observations in GITEAS. For example, in our GITEAS experiment, the reflection probability showed an oscillatory behavior with the increasing incidence angle. The fluctuations observed in TEAS and LEED came with peak-width oscillations and were ascribed to an irregularly stepped surface [8, 29, 30]. However, the comprehensive analysis of the corresponding peak widths showed that the peak width monotonously varied because of the surface curvature. Consequently, surface defects can be excluded as potential factors contributing to the observed intensity variation. Additionally, this analysis benefits the design of atom optical components. Notably, although both w_1 at $\theta_{\text{in}} = 3$ mrad and w_{-1} near $\theta_{R,-1}$ in Fig. 2(a) are sufficiently broad for monochromator applications, only the -1st -order diffraction beam is suitable for this purpose. This is because wavelength-dependent angular dispersion and wavelength-independent grating magnification primarily influence w_{-1} and w_1 , respectively. Furthermore, peak-width analysis is critical in atom interferometry using GITEAS. Overall, our results represent an important step toward the establishment of GITEAS.

This study was supported by NRF (National Research Foundation of Korea) grants funded by the Korean Government (NRF-2020R1A2C3003701 and NRF-2022M3C1C8094518).

L. Y. K. and D. W. K. contributed equally to this work.

* wschoell@fhi-berlin.mpg.de
 † zhao@unist.ac.kr

[1] P. Scherrer, *Göttinger Nachrichten Math. Phys.* **2**, 98 (1918).
 [2] J. I. Langford and A. J. C. Wilson, *J. Appl. Cryst.* **11**, 102 (1978).
 [3] D. Balzar, N. Audebrand, M. R. Daymond, A. Fitch, A. Hewat, J. I. Langford, A. Le Bail, D. Louër, O. Mason, C. N. McCowan, N. C. Popa, P. W. Stephens, and B. H. Toby, *J. Appl. Cryst.* **37**, 911 (2004).
 [4] U. Holzwarth and N. Gibson, *Nat. Nanotechnol.* **6**, 534 (2011).
 [5] D. M. Smilgies, *J. Appl. Cryst.* **42**, 1030 (2009).
 [6] A. Mahmood and J.-L. Wang, *Sol. RRL* **4**, 2000337 (2020).
 [7] D. Farías and K. H. Rieder, *Rep. Prog. Phys.* **61**, 1575 (1998).
 [8] B. Poelsema, R. L. Palmer, G. Mechtersheimer, and G. Comsa, *Surf. Sci.* **117**, 60 (1982).
 [9] B. Poelsema and G. Comsa, eds., *Scattering of thermal energy atoms from disordered surfaces*, Springer tracts in modern physics, Vol. 115 (Springer, Berlin, 1989).
 [10] R. E. Grisenti, W. Schöllkopf, J. P. Toennies, J. R. Manson, T. A. Savas, and H. I. Smith, *Phys. Rev. A* **61**, 033608 (2000).
 [11] P. Kirkpatrick and A. V. Baez, *J. Opt. Soc. Am.* **38**, 766 (1948).
 [12] H. Mimura, S. Handa, T. Kimura, H. Yumoto, D. Yamakawa, H. Yokoyama, S. Matsuyama, K. Inagaki, K. Yamamura, Y. Sano, K. Tamasaku, Y. Nishino, M. Yabashi, T. Ishikawa, and K. Yamauchi, *Nat. Phys.* **6**, 122 (2010).
 [13] H. Yumoto, H. Mimura, T. Koyama, S. Matsuyama, K. Tono, T. Togashi, Y. Inubushi, T. Sato, T. Tanaka, T. Kimura, H. Yokoyama, J. Kim, Y. Sano, Y. Hachisu, M. Yabashi, H. Ohashi, H. Ohmori, T. Ishikawa, and K. Yamauchi, *Nat. Photon.* **7**, 43 (2013).
 [14] H. C. Schewe, B. S. Zhao, G. Meijer, and W. Schöllkopf, *New J. Phys.* **11**, 113030 (2009).
 [15] H. Schief, V. Marsico, K. Kuhnke, and K. Kern, *Surf. Sci.* **364**, L631 (1996).
 [16] V. Druzhinina and M. DeKieviet, *Phys. Rev. Lett.* **91**, 193202 (2003).
 [17] B. S. Zhao, S. A. Schulz, S. A. Meek, G. Meijer, and W. Schöllkopf, *Phys. Rev. A* **78**, 010902 (2008).
 [18] B. S. Zhao, H. C. Schewe, G. Meijer, and W. Schöllkopf, *Phys. Rev. Lett.* **105**, 133203 (2010).
 [19] J. Fiedler, K. Lefmann, W. von Klitzing, and B. Holst, *Phys. Rev. A* **108**, 023306 (2023).
 [20] J. H. Lee, L. Y. Kim, Y.-T. Kim, C. Y. Lee, W. Schöllkopf, and B. S. Zhao, *Phys. Rev. Lett.* **122**, 040401 (2019).
 [21] See Supplemental Material for more details.
 [22] A. Erko, M. Idir, T. Krist, and A. G. Michette, eds., *Modern developments in X-Ray and neutron optics* (Springer, Berlin, 2011).
 [23] J. Als-Nielsen and D. McMorrow, eds., *Elements of modern X-ray physics* (John Wiley & Sons, Ltd, West Sussex, 2011).
 [24] B. S. Zhao, G. Meijer, and W. Schöllkopf, *Phys. Rev. Lett.* **104**, 240404 (2010).
 [25] B. S. Zhao, G. Meijer, and W. Schöllkopf, *New J. Phys.* **13**, 065017 (2011).
 [26] B. E. Saleh and M. C. Teich, *Fundamentals of photonics* (John Wiley & Sons, Ltd, New York, 2019).
 [27] C. Palmer, *Diffraction grating handbook*, 8th ed. (MKS Instruments, Inc., New York, 2020).
 [28] B. Poelsema, G. Mechtersheimer, and G. Comsa, *Surf. Sci.* **111**, 519 (1981).
 [29] M. Henzler, *Appl. Phys.* **9**, 11 (1976).
 [30] M. Henzler, *Surf. Sci.* **73**, 240 (1978).
 [31] W. Schöllkopf, R. E. Grisenti, and J. P. Toennies, *Eur. Phys. J. D* **28**, 125 (2004).

Supplemental Material

Atomic and molecular beam apparatus

A continuous beam was generated by supersonically expanding either He atoms or D₂ molecules through a 5- μm -diameter nozzle. The temperature T_0 and pressure P_0 of the source were set to 9.0 K and 0.5 bar, respectively, for He atoms of $\lambda = 330$ pm and set to $T_0 = 52$ K and $P_0 = 26$ bar, respectively, for He atoms of $\lambda = 140$ pm. To compare the diffractions of the He atomic and D₂ molecular beams of the same λ values, we set the conditions for D₂ molecules to $P_0 = 2$ bar and $T_0 = 52$ K. The λ values were determined from the velocity distributions of the particles.

The beam first passed through a skimmer with a diameter of 500 μm and was subsequently collimated by two slits (S1 and S2) placed 100 cm apart. The widths of these slits, W_{S1} and W_{S2} , were the same (20 μm). The incident and scattered beams were detected by precisely rotating a mass spectrometer with electron-bombardment ionization. The rotational axis of the detector was located 40 cm downstream from S2. Just before the ion detector, a third slit (S3) with a width of $W_{S3} = 25$ μm was positioned to enhance the angular resolution. The distance between the rotational axis and S3, referred to as the grating-detector distance (or detector radius), was $L = 38$ cm. This distance, combined with the narrow aperture of S3, yielded a full width at half maximum (FWHM) of approximately 120 μrad for the collimated incident beam. The grating was carefully positioned and oriented such that the pivot axis of the detector aligned with the center of the grating plane and was maximally parallel to the grating grooves. Therefore, the grating grooves were perpendicular to the plane of incidence defined by the incident wave vector and grating normal, resulting in in-plane diffraction. This geometry is illustrated in Fig. 1 in the main text, where both the incidence angle θ_{in} and detection angle θ are measured in relation to the grating plane.

Velocity distributions of atomic and molecular beams

We obtained the velocity distributions of the He atomic and D₂ molecular beams using time-of-flight measurements conducted with a mechanical pseudo-random beam chopper [31]. Figures S1(a) and S1(b) present the results obtained at temperatures of $T_0 = 9.0$ K and 52 K, respectively. We employed Gaussian function fitting to determine both the mean velocity v and FWHM Δv . The ratios of $\Delta v/v$ for the He atom beams are 0.0075 and 0.0081 at the two different T_0 values, which are similar. In contrast, the ratio $\Delta v/v$ for the D₂ molecular beam is 0.11.

Fabrication and characterization of the diffraction gratings

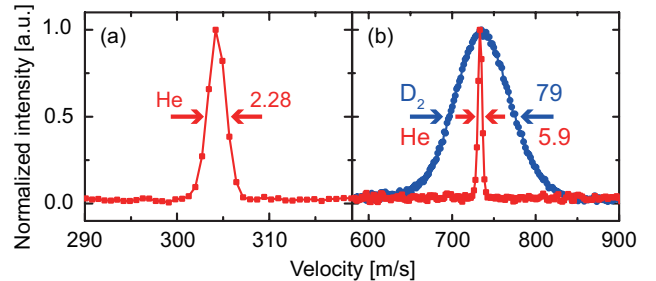


FIG. S1. Measured velocity distributions of He (red squares) and D₂ (blue circles) at (a) $T_0 = 9$ and (b) 52 K. The intensity is scaled to the peak values. Under conditions of $P_0 = 0.5$ bar and 26 bar for $T_0 = 9$ K and 52 K, respectively, the FWHM values for the He atom beams are 2.28 and 5.9 m/s. In contrast, the velocity width of the D₂ molecular beam is 79 m/s at $T_0 = 52$ K. The mean velocities for these distributions are approximately 304 and 730 m/s for $T_0 = 9$ and 52 K, respectively.

We employed three square-wave gratings with varying periods d and strip widths a : G₁ with $d = 1$ μm and $a = 0.25$ μm , G₂₀ with $d = 20$ μm and $a = 10$ μm , and G₄₀₀ with $d = 400$ μm and $a = 200$ μm . G₁ and G₂₀ are microstructured arrays, each measuring 56 mm in length, consisting of 110-nm-thick chromium stripes that are 5 mm in length and are deposited on a 2-mm-thick quartz surface. In contrast, G₄₀₀ is an array featuring parallel photoresist strips with a thickness of 1 μm , width of 200 μm , and length of 4 mm. These strips are located on a commercial gold mirror (Thorlabs PFSQ20-03-M03), which is 6 mm thick and has a surface area of 50.8 \times 50.8 mm². Only the stripes were exposed to the incident atomic beam for all the angles of incidence examined in this study. Table S1 provides a summary of the properties of these gratings that are pertinent to variations in peak width, including their period d and radius of curvature R .

TABLE S1. Grating properties relevant to the peak-width variation

	period	curvature radius
G ₁	1 μm	30 m
G ₂₀	20 μm	-210 m
G ₄₀₀	400 μm	1800 m

Angular spectrum

Figure S2 shows the angular spectrum of the He atom beam diffracted from G₁ at $\theta_{\text{in}} = 5.77$ mrad. The graph represents the He signal as a function of the detection angle θ . A peak in the graph corresponds to a specific diffraction order, indicated by the number above each peak. The specular peak position θ_0 equals $\theta_{\text{in}} = 5.77$. The widths of specular and 1st-order-diffraction peaks

(w_0 and w_1) are 0.31 mrad and 0.21 mrad, respectively.

Experimental conditions

Table S2 lists the five experimental conditions E1–E5 at which the five data sets presented in this study were obtained.

TABLE S2. Experimental conditions employed in this experiment

Particle	Grating	λ_{dB}	T_0	P_0
E1	He	G ₁	330 pm	9.0 K 0.5 bar
E2	He	G ₂₀	330 pm	9.0 K 0.5 bar
E3	He	G ₄₀₀	330 pm	9.0 K 0.5 bar
E4	He	G ₄₀₀	140 pm	52 K 26 bar
E5	D ₂	G ₄₀₀	140 pm	52 K 2.0 bar

Calculation of parameters required for peak-width analysis

For a cylindrically concave mirror with a curvature radius R , the object distance o and image distance i_n of the n th-order beam satisfy the following equation under grazing incidence conditions:

$$\frac{\theta_{\text{in}}^+ - \alpha/2}{o - R\alpha} + \frac{\theta_n^+ + \alpha/2}{i_n + R\alpha} = \frac{2}{R} + \frac{(\theta_{\text{in}}^- - \theta_n^-) + (\theta_{\text{in}}^+ - \theta_n^+)}{W_G/\theta_{\text{in}}}. \quad (\text{S1})$$

Here, θ_{in}^+ and θ_{in}^- represent the outermost values of the incidence angles that result in θ_n^+ and θ_n^- , respectively. The incidence beam spreads over a distance of $W_G/\sin\theta_{\text{in}}$ on the surface. This chord subtends an angle of 2α at the center of curvature, making α approximately equal to $W_G/(2R\sin\theta_{\text{in}})$. Consequently, i_n varies as a function of θ_{in} , as depicted in the first row of Fig. S3 for the five experimental conditions. For our calculations, we assume $R = 30$ m. When $i_n = L$, a diffraction beam is focused on the detection plane. Eq. S1 transforms into the thin-lens equation, $1/o + 1/i_0 = 1/f_0$, for a specular beam

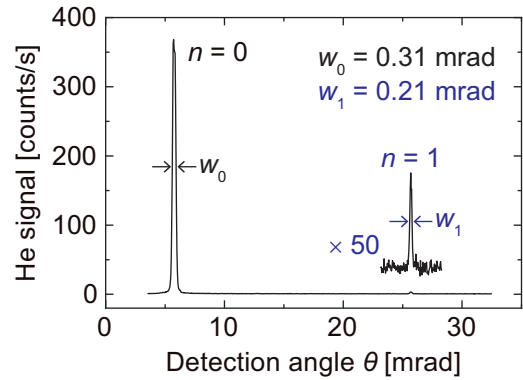


FIG. S2. Angular spectrum of the He atom beam diffracted from G₁ at $\theta_{\text{in}} = 5.77$ mrad (the insets show parts of the spectrum on an enlarged scale).

of $n = 0$ with $f_0 = R\sin\theta_{\text{in}}/2 \simeq R\theta_{\text{in}}/2$ under grazing incidence conditions. Generally, $1/o + 1/i_n = 1/f_n$, with which we obtain f_n using i_n [See Figs. S3(b1–b5)]. Then, $\epsilon_n = 1/L - i_n$. The third row of Fig. S3 shows $|\epsilon_n|$ for the five experimental conditions. To elucidate the contributions of the focusing error ϵ_n and the grating magnification M_n to $W_n^{(1)}$, we plot M_n in the last row of Fig. S3.

Peak-width analysis for G₄₀₀

Similar to Fig. 3 in the main text, Fig. S4 compares the measured W_n (symbols) for G₄₀₀ with the corresponding calculated values: W_n , $W_n^{(1)}$, $W_n^{(2)}$, $W_n^{(3)}$, $W_n^{(4)}$, and $W_n^{(5)}$ (solid lines). The theoretical curves are derived using $R = 1800$ m. In most cases, the primary factor is $W_n^{(1)}$ (red dashed line). Exceptions occur for W_{-1} at the Rayleigh conditions of $\theta_{\text{in}} = \theta_{R,-1}$. At these conditions, θ_{-1} approaches 0, leading to large values for $W_{-1}^{(2)}$, $W_{-1}^{(3)}$, and $W_{-1}^{(4)}$.

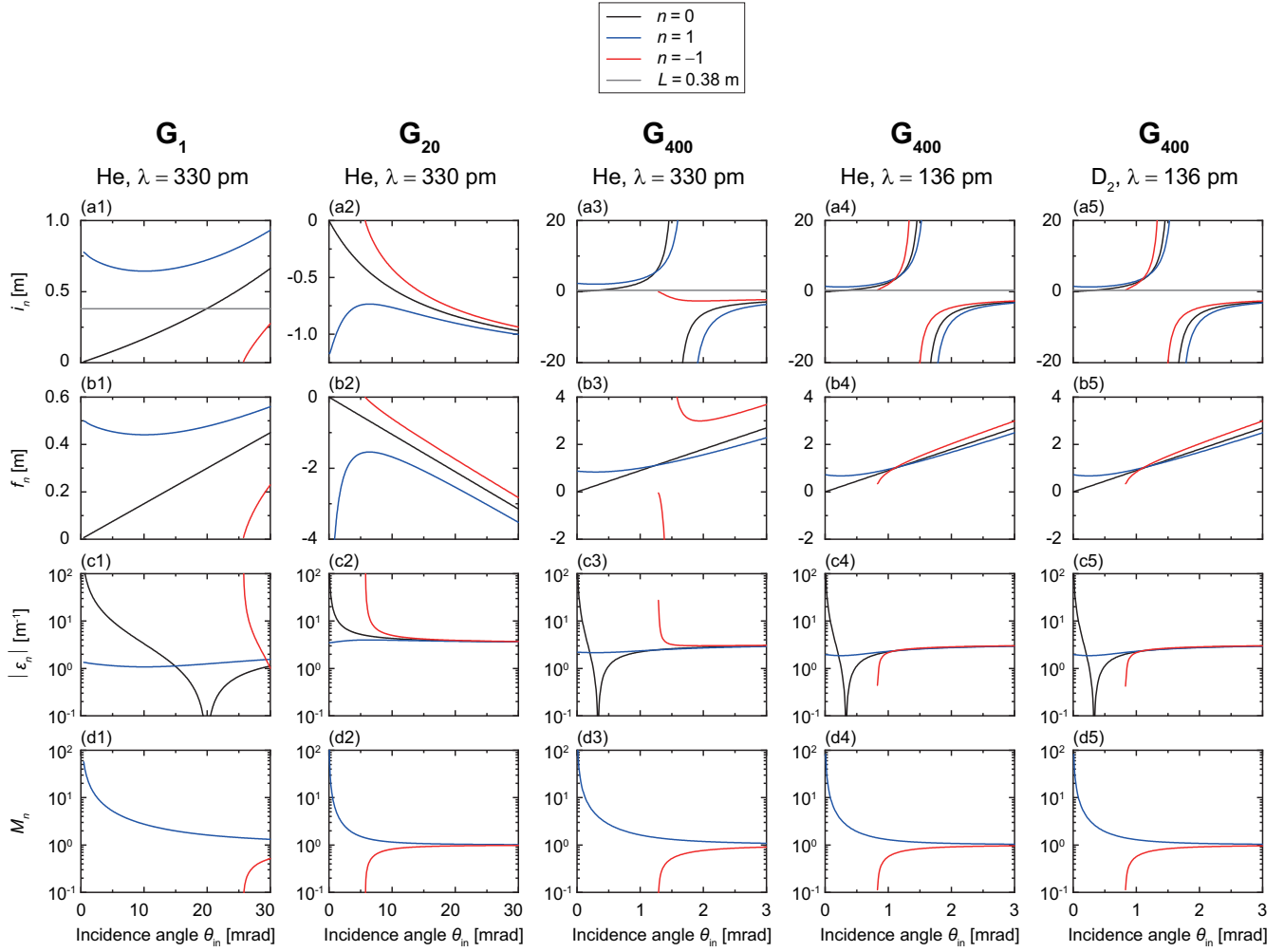


FIG. S3. (a1–a5) Image distance i_n , (b1–b5) focal length f_n , (c1–c5) focusing error ϵ_n , and grating magnification M_n of the n th-order diffraction beam. The five columns correspond to the experimental conditions outlined in Table S2, respectively. Here, \mathbf{G}_1 , \mathbf{G}_{20} , and \mathbf{G}_{400} are assumed to be cylindrical mirrors with curvature radii of $R = 30$, -210 , and 1800 m, respectively. These graphs are plotted as functions of the incidence angle θ_{in} . The horizontal dotted line in “(a1–a5)” indicates the grating–detector distance $L = 0.38$ m.

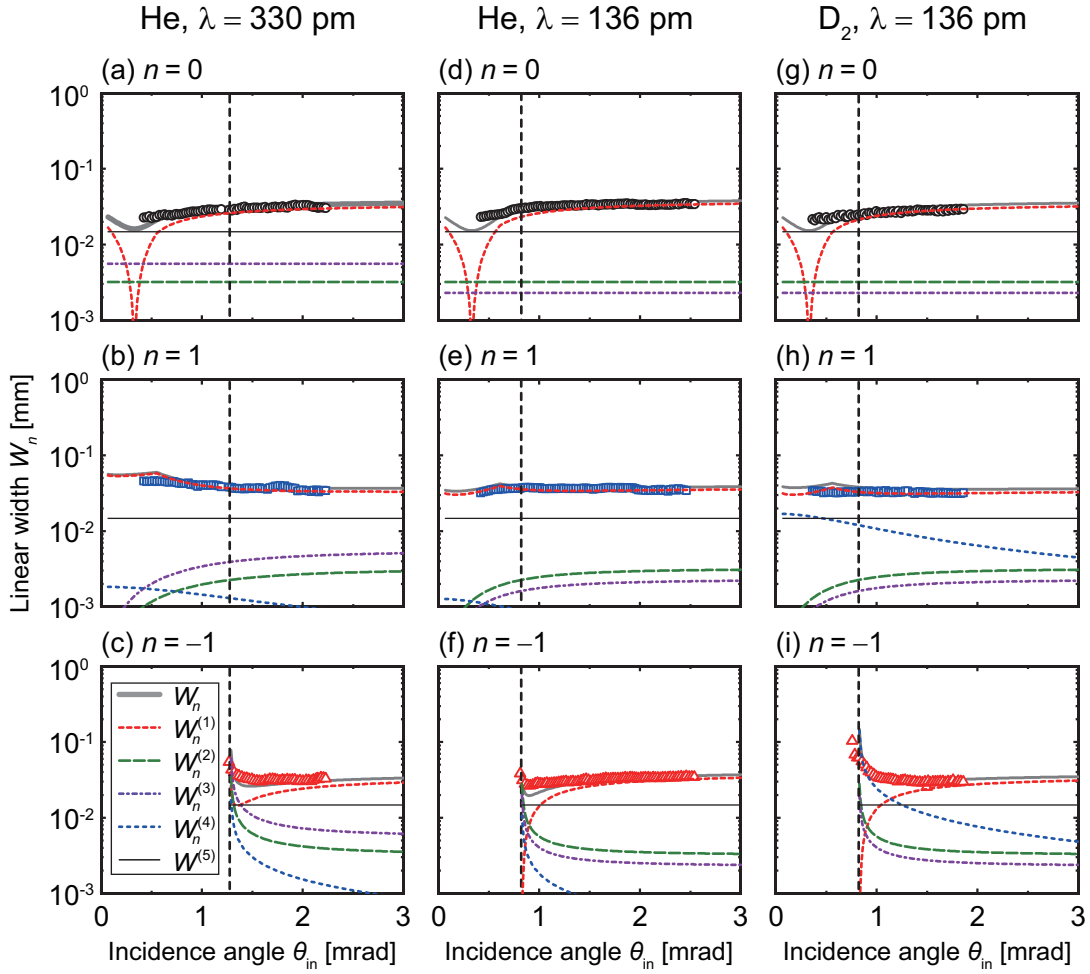


FIG. S4. Comparison between the measured (symbols) and calculated (solid curves) linear widths W_n of the n th-order diffraction beam from G_{400} . The graphs in the three columns correspond to the experimental conditions E3, E4, and E5 as listed in Table S2, respectively. The data are presented sequentially from the top for $n = 0, 1$, and -1 . Specifically, W_0 , W_1 , and W_{-1} are individually plotted alongside the calculated values $W_n^{(1)}$, $W_n^{(2)}$, $W_n^{(3)}$, $W_n^{(4)}$, and $W_n^{(5)}$.